Global and regional patterns of soil nitrous acid emissions and their acceleration of rural photochemical reactions

Dianming Wu[1], Jingwei Zhang[2], Mengdi Wang[1], Junling An[3], Ruhai Wang[4], Haroon Haider[1], – Xu-Ri[5], Ye Huang[1], Qiang Zhang[6], Feng Zhou[7], Hanqin Tian[8], Xiuying Zhang[9], Lingling Deng[1], Yuepeng Pan[10], Xi Chen[1], Yuanchun Yu[1], Chunsheng Hu[11], Rui Wang[1], Yaqi Song[1], Zhiwei Gao[1], Yue Wang[1], Lijun Hou[1], and Min Liu[1]

[1]East China Normal University
[2]The Institute of Atmospheric Physics, CAS, LAPC, Beijing, 100029, P.R.China
[3]Institute of Atmospheric Physics,Chinese Academy of Sciences
[4]Institute of soil Sciences, Chinese Academy of Sciences
[5]Institute of Tibetan Plateau Research, Chinese Academy of Sciences, ,
[6]Tsinghua University
[7]Peking University
[8]Auburn University
[9]International Institute for Earth System Science
[10]State Key Laboratory of Atmospheric Boundary Layer Physics and Atmospheric Chemistry, Institute of Atmospheric Physics, Chinese Academy of Sciences, Beijing, China
[11]Chinese Academy of Sciences (CAS)

November 22, 2022

Abstract

Abiotic and biotic releases of nitrous acid (HONO) from soils contribute substantially to the missing source of tropospheric HONO and hydroxyl radicals (OH). However, global and regional patterns of soil HONO emissions are rarely quantified, and the contributions of such emissions to atmospheric oxidization capacity are unclear. Here, we present that the best estimate of global soil HONO emissions in 2017 is 9.67 with a range of 7.36-11.99 Tg N yr-1, where cropland soils accounted for ˜ 79%. The analyses also indicate that regional soil HONO emissions enhanced ground OH concentrations by 10-60% and ozone concentrations by 0.5-1.5 ppb at daytime in the ambient area of Shanghai, China. The impact of soil HONO emissions on OH budgets were more important in rural than urban areas. These findings suggest that the global soil HONO emissions, especially from cropland, could quicken photochemical reactions and aggravate air pollution in rural areas.

Hosted file

`essoar.10509778.1.docx` available at https://authorea.com/users/540270/articles/600176-global-and-regional-patterns-of-soil-nitrous-acid-emissions-and-their-acceleration-of-rural-photochemical-reactions

Hosted file

`table s1.docx` available at https://authorea.com/users/540270/articles/600176-global-and-regional-patterns-of-soil-nitrous-acid-emissions-and-their-acceleration-of-rural-photochemical-reactions

Hosted file

si_1220.docx available at https://authorea.com/users/540270/articles/600176-global-and-regional-patterns-of-soil-nitrous-acid-emissions-and-their-acceleration-of-rural-photochemical-reactions

Global and regional patterns of soil nitrous acid emissions and their acceleration of rural photochemical reactions

Dianming Wu[1,2,†,*], Jingwei Zhang[3,4,†], Mengdi Wang[1,2,†], Junling An[3,4,*], Ruhai Wang[5], Haroon Haider[1,2], Xu-Ri[6,7], Ye Huang[1,2], Qiang Zhang[8,9], Feng Zhou[10], Hanqin Tian[11], Xiuying Zhang[12], Lingling Deng[1,2], Yuepeng Pan[3], Xi Chen[1], Yuanchun Yu[13], Chunsheng Hu[14], Rui Wang[1,2], Yaqi Song[1,13], Zhiwei Gao[1,2], Yue Wang[1,2], Lijun Hou[15], Min Liu[1,2,*]

[1]Key Laboratory of Geographic Information Science (Ministry of Education), School of Geographic Sciences, East China Normal University, Shanghai, China.
[2]Institute of Eco-Chongming (IEC), Shanghai, China.
[3]State Key Laboratory of Atmospheric Boundary Layer Physics and Atmospheric Chemistry (LAPC), Institute of Atmospheric Physics (IAP), Chinese Academy of Sciences, Beijing, China.
[4]College of Earth and Planetary Sciences, University of Chinese Academy of Sciences, Beijing, China.
[5]State Key Laboratory of Soil and Sustainable Agriculture, Institute of soil Sciences, Chinese Academy of Sciences, Nanjing, China.
[6]Key Laboratory of Alpine Ecology and Biodiversity, Institute of Tibetan Plateau Research, Chinese Academy of Sciences, Beijing, China.
[7]CAS Center for Excellence in Tibetan Plateau Earth Sciences, Beijing, China.
[8]Ministry of Education Key Laboratory for Earth System Modeling, Department of Earth System Science, Tsinghua University, Beijing, China.
[9]Collaborative Innovation Center for Regional Environmental Quality, Beijing, China.
[10]Sino-France Institute of Earth Systems Science, Laboratory for Earth Surface Processes, College of Urban and Environmental Sciences, Peking University, Beijing, China.
[11]International Center for Climate and Global Change Research and School of Forestry and Wildlife Sciences, Auburn University, Auburn, USA.
[12]International Institute for Earth System Science, Nanjing University, Nanjing, China.
[13]Co-Innovation Center for the Sustainable Forestry in Southern China, College of Biology and the Environment, Nanjing Forestry University, Nanjing, China.
[14]Key Laboratory of Agricultural Water Research, Center for Agricultural Resources Research, Institute of Genetic and Developmental Biology, Chinese Academy of Sciences, Shijiazhuang, China.
[15]State Key Laboratory of Estuarine and Coastal Research, East China Normal University, Shanghai, China.

Corresponding author: Dianming Wu (dmwu@geo.ecnu.edu.cn); Junling An (anjl@mail.iap.ac.cn); Min Liu (mliu@geo.ecnu.edu.cn)

† Dianming Wu, Jingwei Zhang, and Mengdi Wang contributed equally to this work.

Key Points:

- The best estimate of global soil HONO emissions in 2017 is 9.67 with a range of 7.36-11.99 Tg N yr^{-1}, where cropland soils accounted for ~ 79%.

- Soil HONO emissions enhanced ground OH concentrations by 10-60% and ozone concentrations by 0.5-1.5 ppb at daytime.

- The impact of soil HONO emissions on OH budgets were more important in rural than urban areas.

Abstract

Abiotic and biotic releases of nitrous acid (HONO) from soils contribute substantially to the missing source of tropospheric HONO and hydroxyl radicals (OH). However, global and regional patterns of soil HONO emissions are rarely quantified, and the contributions of such emissions to atmospheric oxidization capacity are unclear. Here, we present that the best estimate of global soil HONO emissions in 2017 is 9.67 with a range of 7.36-11.99 Tg N yr^{-1}, where cropland soils accounted for ~ 79%. The analyses also indicate that regional soil HONO emissions enhanced ground OH concentrations by 10-60% and ozone concentrations by 0.5-1.5 ppb at daytime in the ambient area of Shanghai, China. The impact of soil HONO emissions on OH budgets were more important in rural than urban areas. These findings suggest that the global soil HONO emissions, especially from cropland, could quicken photochemical reactions and aggravate air pollution in rural areas.

1 Introduction

Reactive nitrogen (N_r) gases released from the land surface strongly affect the Earth's atmosphere through atmospheric cycling of hydroxyl radicals (OH) and ozone (O_3) (Crutzen, 1970; Elshorbany et al., 2012; Liang et al., 1998; Pinder et al., 2012). While soil emissions of nitrous acid (HONO) have been recently reported (Oswald et al., 2013; Su et al., 2011; Wu et al., 2019), the associated global patterns and impacts on air quality are poorly defined. Lacking data on global and regional soil HONO emissions and accurate assessments of atmospheric oxidation capacity limit our understanding of atmospheric HONO sources and sinks, OH recycling, the formation of secondary aerosols and O_3, and biogeochemical N cycling.

Soil HONO emissions were studied to explain the unknown daytime atmospheric HONO sources in many regions, such as Meusel et al. (2018) and Sörgel et al. (2015). The proposed underlying mechanisms include chemical equilibrium with soil nitrite (NO_2^-) (Su et al., 2011), microbiological nitrification or denitrification pathways (Oswald et al., 2013; Wu et al., 2019), soil mineral surface acidification caused by amphoteric metal oxides or nitrate accumulation (Donaldson et al., 2014; Kim & Or, 2019), and acid displacement (VandenBoer et al., 2015). Moreover, the emission rates of soil HONO are comparable to those of nitric oxide (NO) measured in laboratory (Oswald et al., 2013; Weber et al., 2015). Soil NO emissions have been widely studied globally and regionally by both bottom-up and top-down models (Bertram et al., 2005; Ganzeveld et al., 2002; Yienger & Levy II, 1995). The IPCC (Ciais et al., 2013) and other studies (Hudman et al., 2012; Miyazaki et al., 2017; Steinkamp & Lawrence, 2011; Vinken et al., 2014; Yan et al., 2005; Yienger & Levy II, 1995) reported a broad range of global soil nitrogen oxide [NO_x = NO + nitrogen dioxide (NO_2)] emissions of 4.7-16.8 Tg yr^{-1} (in terms of nitrogen, hereinafter referred to as Tg N yr^{-1}). The large uncertainties might be caused by specific parameters, including emissions factors, land cover maps, the impact of precipitation on NO_x emissions assumed in semi-empirical models, and the uncertain relationship between observed NO_2 concentrations and soil NO_x emissions using the Ozone Monitoring Instrument (OMI) model (Rasool et al., 2019; Steinkamp & Lawrence, 2011).

However, the estimation of soil HONO emissions is rare either at the global or regional scale due to a lack of data and appropriate method. Wu et al. (2019) estimated that global soil HONO emissions at high moisture ranged from 0.03-0.20 Tg N yr^{-1}, while the estimated global

86   HONO emissions from biological soil crusts in drylands were approximately 0.6 ± 0.1 Tg N yr^{-1}
87   (Weber et al., 2015). A process-oriented representation of soil N emissions in the Community
88   Multiscale Air Quality model (CMAQ) was developed to simulate soil HONO emissions based
89   on the proportions of HONO relative to total NO_x in the United States (Rasool et al., 2019). The
90   monthly average emission rates of soil NO and HONO were highest in fertilized agricultural
91   regions with large spatial and temporal heterogeneity (Rasool et al., 2019). An estimation of
92   global natural and cropland soil HONO emissions has not been reported.

93   Atmospheric HONO sources are not well understood, and the default HONO formation
94   mechanism (NO+OH→HONO) always severely underestimates HONO observations and
95   atmospheric oxidation capacity as a result. Several potential HONO sources (traffic emissions,
96   NO_2 heterogeneous reactions, etc.) have been coupled into regional chemical transport models
97   (e.g., the Weather Research and Forecasting model with Chemistry (WRF-Chem) and CMAQ).
98   The results showed that potential HONO sources could significantly enhance atmospheric
99   oxidation capacity and lead to increases in the concentrations of fine particulate matter ($PM_{2.5}$),
100   O_3, and secondary organic aerosols (SOA) (Li et al., 2010; Zhang et al., 2019; Zhang et al.,
101   2016). Although soil HONO emissions have been included in the chemical transport model in
102   recent years (Wang et al., 2021; Zhang et al., 2019; Zhang et al., 2016), large uncertainties in soil
103   HONO emissions remain.

104   Here, we compiled a dataset of global soil samples related to HONO emissions and
105   estimated global soil HONO emissions with a resolution of $0.1° \times 0.1°$ using an empirical
106   "wetting-drying" model. Soil NO and NO_x emissions were also calculated to verify the method
107   accuracy by comparison with reported values. A statistical model was also used to calculate
108   global soil HONO emissions. The simulations of global and regional chemical transport models
109   are similar, but it is very difficult to evaluate the global model performance in terms of simulated
110   HONO values due to extremely limited global HONO observations in the same period. Thus, we
111   used the regional WRF-Chem model to quantify the impacts of local soil HONO emissions on
112   the concentrations of atmospheric HONO, OH and O_3 in Shanghai, China, and its surrounding
113   areas. The model may perform well elsewhere too for future related studies. Comprehensive
114   measurements of soil HONO flux were conducted in this study, and abundant
115   environmental/meteorological observations were collected for model validation.

116   **2 Materials and Methods**

117   2.1 Soil samples

118   We compiled a dataset of global soil sample data published in different studies related to
119   soil HONO emissions (S11-S21, S33-S44, S55-S64, and S67-S78; see Figure S1 and Table S1).
120   Parts of soil physicochemical properties were collected from cited references, while other soil
121   properties were derived from different sources. Soil inorganic nitrogen (NH_4^+, NO_2^-, and NO_3^-)
122   contents were obtained from Xu-Ri & Prentice (2008), pH, TC, TOC, and TN values were
123   downloaded from the Global Soil Dataset for use in Earth System Models (GSDE) (Shangguan
124   et al., 2014), and soil texture data (clay, silt, and sand) were obtained from the Harmonized
125   World Soil Database (HWSD) v 1.2. We used data from these soil samples together with soil

126 samples from Shanghai, China (see details in the following information), to estimate global and
127 regional soil emissions of HONO.

128   We took 35 soil samples (S1-S10, S22-S32, S45-S54, S65, S66, S77, and S78) from
129 different land cover types of Shanghai during July 2018. The sampling sites are located in
130 eastern China (120°52'E-122°12'E, 30°40'N-31°53'N) with a typical subtropical humid monsoon
131 climate. The mean annual temperature, precipitation and sunshine hours were 17.7 °C, 1388.8
132 mm and 1809.2 h, respectively, in 2017. All of the samples were taken from the upper layer of
133 the soil (0-5 cm). Each sample was separated into two parts: one part was stored at -20 °C and
134 used to measure soil water content, particle size distribution and inorganic nitrogen; the other
135 part was air-dried at room temperature (~ 25 °C), sieved to 2 mm for measuring soil pH and soil
136 HONO, NO, and NO_x flux, and sieved to 0.15 mm for measuring soil TN and TC. Figure S1 and
137 Table S1 provide more detailed information about the soils.

138   Soil pH was measured using a glass electrode (FE28, Mettler-Toledo) after shaking a soil
139 and water suspension at a ratio of 1:2.5 (weight/volume, w/v) for 30 min. Soil water content was
140 calculated through the drying method (105 °C, 24 h). Inorganic nitrogen was extracted with 2
141 mol L^{-1} potassium chloride (KCl, 1:2.5 w/v) and then determined by a continuous flow analyser
142 (Skalar San++ System, Skalar). Soil TC, TOC and TN were measured by a TOC-L analyser
143 (TOC-L, Shimadzu). Soil particle size was analysed using a laser diffraction particle size
144 analyser (LA-960A, HORIBA).

145   2.2 HONO, NO, and NO_x flux measurements

146   Soil N_r gas flux was measured with a dynamic chamber system, which has been
147 described in detail elsewhere (Wu et al., 2019). Previous studies showed that this technique can
148 well simulate reactive gas flux from field measurements (Plake et al., 2015; Rummel et al., 2002;
149 van Dijk et al., 2002). Briefly, 40 grams of air-dried soil was put into a petri dish (inner diameter
150 = 94 mm) and wetted with purified water to the water holding capacity (WHC, %). Then, the
151 petri dish was placed into a Teflon chamber (volume ~ 10 L) with a fan coated with Teflon to
152 mix the gases inside the chamber. Purified air without water and reactive gases (such as HONO,
153 NO_x, O_3, and C_xH_y) were flushed into the chamber with a flow rate of 6 L min^{-1}. Thus, the
154 wetted soil in the chamber was dried during measurements, which was defined as a full wetting-
155 drying cycle when no water vapor was detected in the chamber. The mixing ratio of HONO in
156 the headspace was determined by high-performance liquid chromatography (HPLC, Agilent
157 1200, Agilent Technologies) based on the derivatization of nitrite with sulfanilamide (SA) and
158 N-(1-naphthyl)-ethylenediamine dihydrochloride (NED) under acidic conditions (Huang et al.,
159 2002; Wu et al., 2020). The time resolution was ~ 6 min, and the lower detection limit was ~ 4
160 ppt for HONO. The mixing ratios of NO and NO_2, CO_2, and H_2O in the headspace were
161 determined by a NO_x chemiluminescence analyzer (Model 42iTL, Thermo Scientific), an ozone
162 analyser (Model 49i, Thermo Scientific), and a LI-COR (Model 840A, LI-COR), respectively.
163 Due to the overestimation by the chemiluminescence analyzer, NO_2 data were corrected by
164 multiplying by 0.6, which was from the relationship of measured NO_2 concentrations between
165 the chemiluminescence analyzer and an improved incoherent broadband cavity-enhanced
166 absorption spectroscopy (IBBCEAS) system (Tang et al., 2020). All of the experiments were

167 conducted at a constant temperature of 25 °C in the dark. The fluxes of HONO, NO, and NO$_x$
168 were calculated using equation 1:

169 $$F = \frac{Q*M_N}{A*V_m} * X \qquad (1)$$

170 where F is the flux of reactive nitrogen gas (ng N m^{-2} s^{-1}). Q is the chamber air flow rate
171 (m^3 s^{-1}). M_N is the molar mass of nitrogen (g mol^{-1}). A is the area of the soil surface (m^2). V_m is
172 the molar volume under standard reference atmospheric conditions (m^3 mol^{-1}). X is the headspace
173 concentration of N$_r$ gas (ppb).

174 2.3 Integrated soil N$_r$ gas emissions per wetting-drying cycle

175 Integrated emissions of HONO, NO, and NO$_x$ from Shanghai soils during a full wetting-
176 drying cycle were calculated according to equation 2:

177 $$E_{N,int} = \sum_{i=0}^{i=max} F_i * (t_i - t_{i-1}) * 10^{-6} \qquad (2)$$

178 where $E_{N,int}$ is the integrated emission of N$_r$ gas (mg N m^{-2}). t_i is the measurement time
179 for i. F_i is the flux of N$_r$ gas at t_i (ng N m^{-2} s^{-1}). Supplementary Text S1 and Figure S2 show more
180 information about the results.

181 We also collected data on integrated soil HONO, NO, and NO$_x$ emissions from various
182 ecosystems (see Supplementary Text S1, Table S1 and Figure S2). Then, we calculated the
183 integrated emissions of HONO, NO, and NO$_x$ from different land cover types per wetting-drying
184 cycle ($E_{N,int,LC}$, mg N m^{-2}; average ± standard error) (for specific values, see Supplementary Text
185 S1). The land cover types (LC), including cropland (CR), forest (FR), grassland (GL), shrubland
186 (SL), wetland (WL), and bare land (BL), were classified according to Gong et al. (2019). Natural
187 vegetation (NV) was defined as all of the land cover types except cropland. We adjusted the
188 spatial resolution of the land cover map to 0.1° × 0.1° to be consistent with the precipitation data.

189 2.4 Upscaling soil emissions of N$_r$ gases to global scale

190 We estimated global soil HONO, NO, and NO$_x$ emissions based on the empirical
191 "wetting-drying method" as described by Weber et al. (2015), which showed consistent results
192 with those estimated by a process-based modelling approach (Porada et al., 2019).

193 First, the N$_r$ emissions per grid cell containing different land cover types induced by
194 precipitation and temperature ($E_{LC,cell}$, kg N ha^{-1} yr^{-1}) could be obtained according to equation 3:

195 $$E_{LC,cell} = E_{N,int,LC} * P_{cell} * T_{cal} * 10^{-2} \qquad (3)$$

196 where P_{cell} represents the number of precipitation events for each grid cell during one
197 year; one precipitation event was defined by a daily rainfall at the central point > 0.1 mm. The
198 one-day multi-satellite precipitation data were obtained from NASA and had a spatial resolution
199 of 0.1° × 0.1° (Huffman et al., 2019). T_{cal} represents the calibration factor of temperature
200 (Hudman et al., 2012), which can be calculated by the following equation 4:

201 $$T_{cal} = e^{0.103*T}/(Q_{10} * 2.5) \qquad (4)$$

202 where T is monthly averaged soil surface (0-7 cm) temperature (°C) from the datasets of
203 ERA5-Land (Muñoz Sabater, 2019), Q_{10} is temperature coefficient (Winkler et al., 1996) and the
204 value is calculated and averaged based on soil flux of HONO, NO, and NO$_x$ at different

205 temperature from the data of Wu et al. (2019) and Oswald et al. (2013). 2.5 is the calibrated
206 constant of soil temperature.

207 Then, the fertilizer-induced direct emissions from cropland per grid cell ($E_{fer,cell}$, kg N ha^{-1}
208 yr^{-1}) were added using the emission factor method according to equation 5:

209 $$E_{fer,cell} = F_{cell} * EF * 10^{-2} \tag{5}$$

210 where F_{cell} is the amount of fertilizer input in different grid cells (kg N ha^{-1} yr^{-1}) and was
211 obtained from the National Bureau of Statistics of China (2018) and the Food and Agriculture
212 Organization of the United Nations (FAO, 2017). *EF* is the emission factor (%) induced by
213 fertilization. The value of the *EF*s were described in details in Text S2.

214 Soil HONO, NO, and NO$_x$ emissions from different land cover types caused by
215 precipitation and fertilization ($E_{LC,Nr}$ and $E_{fer,Nr}$, Tg N yr^{-1}) were calculated according to
216 equations 6 and 7:

217 $$E_{LC,Nr} = \sum_{i=1}^{n} E_{LC,cell} * A * 10^{-9} \tag{6}$$
218 $$E_{fer,Nr} = \sum_{j=1}^{m} E_{fer,cell} * A * 10^{-9} \tag{7}$$

219 where i is the number of grid cells of different land cover types and j is the number of
220 grid cells of cropland. A is a constant representing the area of each grid cell (~ 12,321 hectares).

221 Finally, we calculated the global or regional soil HONO, NO, and NO$_x$ emissions ($E_{GR, Nr}$,
222 Tg N yr^{-1}) above plant canopy using equation 8:

223 $$E_{GR,Nr} = \left(E_{CR,Nr} + E_{FR,Nr} + E_{GL,Nr} + E_{SL,Nr} + E_{WL,Nr} + E_{BL,Nr} + E_{fer,Nr}\right) * CRF \tag{8}$$

224 where $E_{GR,Nr}$ represents the global soil N$_r$ emissions $E_{global,Nr}$ or different regional soil N$_r$
225 emissions $E_{regional,Nr}$ (see Table 1). *CRF* represents the canopy reduction factor, which can be
226 calculated using equation 9:

227 $$CRF = \left(\frac{e^{-(k_s * SAI)} + e^{-(k_c * LAI)}}{2}\right) \tag{9}$$

228 where k_s and k_c are absorptivity constants of plant leaves and set as 8.75 and 0.24 m^2 m^{-2}
229 (Yienger & Levy II, 1995). *LAI* represents leaf area index, which is obtained from the database
230 of NOAA Global Inventory Monitoring and Modeling System (GIMMS) (Zhu et al., 2013). *SAI*
231 represents stomatal area index, which is calculated based on the value of *LAI*/*SAI* under different
232 land cove types (Yienger & Levy II, 1995). The ranges of global and regional soil HONO, NO,
233 and NO$_x$ emissions were calculated based on the minimum and maximum values of $E_{N,int,LC}$ (see
234 Supplementary Text S1).

235 2.5 Impacts of soil HONO emissions on air quality

236 The soil HONO emissions of the 35 soil samples from Shanghai and the improved WRF-
237 Chem model 3.7.1 were used to evaluate the impact of soil HONO emissions on atmospheric
238 HONO, OH and O$_3$ concentrations. Two domains were adopted in this study: domain 1 covered
239 eastern China and contained 71×71 grid cells with a horizontal resolution of 27 km, and domain
240 2 covered Shanghai and its surrounding regions and contained 45×45 grid cells with a horizontal
241 resolution of 9 km. Shanghai is located in the center of domain 2; the blue dot is the HONO
242 observation site, the 8 black dots (urban) and 1 red dot (rural) are the O$_3$ and NO$_2$ observation
243 sites, and the 26 purple dots are meteorological sites. Detailed locations of the 36 sites are given

244 in Table S2. The physical and chemical options in the WRF-Chem model used in this study are
245 given in Table S3.

246   A previous study showed a strong positive correlation (r = 0.93) between field soil
247 HONO flux and solar radiation and found that the fluxes were quite small at nighttime and
248 strongest at noontime (Xue et al., 2019)**.** Thus, we revised the soil HONO flux measured by the
249 dynamic chamber system based on this relationship (see equation 10) and inserted it into our
250 model.

251
$$F_{(\text{RHONO,LC})} = \frac{SR}{IA} * E_{\text{N,int}} * 10^6 * \frac{1}{3600} \qquad (10)$$

252   where $F_{(\text{RHONO,LC})}$ represents the revised soil HONO flux (ng N $m^{-2}\,s^{-1}$) for a certain land
253 cover type (including cropland, forest, grassland, and urban green land), SR denotes the direct
254 solar radiation intensity (W m^{-2}), IA represents the integrated energy per area during daytime (W
255 h m^{-2}), and $E_{\text{N,int}}$ is the integrated soil HONO emissions (mg N m^{-2}) per wetting-drying process.

256   Equation 10 was established under three assumptions: (1) the integrated soil HONO
257 emissions during the wetting-drying period were the optimum amount; (2) a typical soil wetting-
258 drying period lasted for one day after rainfall; and (3) the optimum amount of soil HONO
259 emissions was only reached on sunny days with the strongest solar radiation (noontime radiation
260 intensity of ~ 900 W m^{-2}, integrated energy of ~ 6000 W h m^{-2}, and daytime radiant energy of ~
261 2.16×10^7 J m^{-2}). For cloudy days with weaker solar radiation, the emissions were reduced
262 according to the radiant energy ratio; i.e., a daytime radiant energy of 1.08×10^7 J m^{-2}
263 corresponded to 50% of the maximum amount for a cloudy day with a wetting-drying process.

264   In total, 10 cases were conducted in this study, i.e., base, soil-A, soil-B, soil-C, 5S-A, 5S-
265 B, 5S-C, base-low, soil-low, and 5S-low cases. The base case only considered the gas-phase
266 production of HONO (NO+OH→HONO). The soil-A case added averaged soil HONO
267 emissions. The 5S-A case added 5 potential HONO sources (5S), including traffic HONO
268 emissions, biomass burning emissions, NO_2 heterogeneous reactions on aerosol and ground
269 surfaces, and average soil HONO emissions. The other 7 cases were designed to evaluate the
270 uncertainties of soil HONO emissions and the effects of anthropogenic NO_x emissions on
271 atmospheric oxidation capacity and O_3 concentrations. A detailed description and
272 parameterizations can be found in our previous work (Zhang et al., 2019) and Tables S4 and S5.

273   Due to the lack of atmospheric HONO observations during the period of soil sampling in
274 Shanghai, another set of field HONO observations in Shanghai reported by Bernard et al. (2016)
275 was collected to evaluate the model performance in terms of HONO simulation. The HONO
276 observations were collected from October 16-24, 2009. Thus, we conducted the base and 5S-A
277 cases focusing on general HONO simulations in the period of October 16-24, 2009, and all 10
278 cases focused on soil HONO emissions in the period of March 2016. Our results showed that the
279 five potential HONO sources could significantly improve HONO simulations and reasonably
280 reproduce observations (Figure S3). The simulated and observed meteorological factors and
281 NO_2/O_3 concentrations were also comparable (see more details in Supplementary Text S3,
282 Figures S4 and S5, and Table S6).

283   Two anthropogenic emission inventories were adopted in this study. The MIX (2010)
284 inventory from Li et al. (2017) was used for the simulations in 2009. The MEIC inventory from
285 Li et al. (2017) and updated to 2016 was used for the simulations in 2016. The horizontal

286   resolutions of the two inventories were 0.5° and 0.25°, respectively. Detailed information on the
287   inventories can be found in our previous work (Zhang et al., 2019).

3 Results and Discussions

289   3.1 Global and regional patterns of soil HONO emissions using an empirical "wetting-
290   drying" model

291   The best estimate of global soil emissions of HONO above plant canopy in 2017 was
292   9.67 (minimum-maximum estimates: 7.36-11.99) Tg N yr^{-1}, consisting of 7.65 (6.30-9.01) and
293   2.02 (1.06-2.97) Tg N yr^{-1} from cropland and natural vegetation, respectively (Table 1). Asia was
294   the largest contributor (average estimate: 4.70 Tg N yr^{-1}) among the continents, accounting for ~
295   49% of global soil HONO emissions, followed by Africa (2.02 Tg N yr^{-1}), South America (1.32
296   Tg N yr^{-1}), North America (0.83 Tg N yr^{-1}), Europe (0.52 Tg N yr^{-1}), and Oceania (0.23 Tg N yr^{-1}) (Table 1). Figure 1a shows the global spatial distribution of soil HONO emissions above
298   canopy. The global average soil emissions of HONO were 0.64 (0.49-0.80) kg N ha^{-1} yr^{-1}. The
299   hotspot areas of soil emissions of HONO were mainly from croplands, including in the South and
300   East Asia, the middle of North and South America and Africa, and Europe.

301   Table 1. Global and regional soil emissions of HONO, NO, and NO$_x$ (E_{HONO}, E_{NO}, and E_{NOx})
302   above plant canopy.

Regions	Sources	Above canopy emissions (Tg N yr^{-1})		
		E_{HONO}	E_{NO}	E_{NOx}
Global	Cropland	7.65 (6.30-9.01)[a]	9.42 (7.68-12.18)	12.03 (10.42-13.64)
	Natural vegetation	2.02 (1.06-2.97)	4.35 (2.32-6.39)	7.11 (2.86-11.36)
	Total	9.67 (7.36-11.99)	13.78 (9.99-18.57)	19.14 (13.28-25.00)
Africa	Cropland	1.56 (1.28-1.83)	1.78 (1.47-2.09)	2.11 (1.79-2.44)
	Natural vegetation	0.47 (0.27-0.67)	1.37 (0.88-1.86)	2.10 (1.07-3.13)
	Total	2.02 (1.55-2.50)	3.15 (2.36-3.95)	4.22 (2.86-5.57)
North America	Cropland	0.60 (0.49-0.72)	0.78 (0.66-0.91)	1.01 (0.87-1.14)
	Natural vegetation	0.23 (0.12-0.34)	0.43 (0.21-0.65)	0.71 (0.28-1.14)
	Total	0.83 (0.61-1.06)	1.21 (0.87-1.55)	1.71 (1.15-2.28)
South America	Cropland	0.70 (0.57-0.83)	0.87 (0.73-1.02)	1.07 (0.92-1.23)
	Natural vegetation	0.62 (0.31-0.94)	1.13 (0.55-1.70)	1.82 (0.67-2.96)
	Total	1.32 (0.88-1.77)	2.00 (1.28-2.72)	2.89 (1.59-4.19)
Asia	Cropland	4.24 (3.50-4.98)	5.32 (4.26-7.39)	6.99 (6.11-7.87)
	Natural vegetation	0.46 (0.23-0.68)	0.83 (0.33-1.33)	1.49 (0.41-2.58)
	Total	4.70 (3.73-5.66)	6.15 (4.59-8.72)	8.48 (6.52-10.45)
Europe	Cropland	0.44 (0.36-0.52)	0.56 (0.47-0.65)	0.72 (0.62-0.81)
	Natural vegetation	0.09 (0.04-0.13)	0.15 (0.07-0.23)	0.24 (0.09-0.40)
	Total	0.52 (0.40-0.65)	0.71 (0.54-0.87)	0.96 (0.71-1.21)
Oceania	Cropland	0.08 (0.07-0.10)	0.10 (0.09-0.12)	0.13 (0.11-0.15)
	Natural vegetation	0.15 (0.09-0.21)	0.45 (0.26-0.63)	0.74 (0.34-1.15)
	Total	0.23 (0.16-0.31)	0.55 (0.35-0.75)	0.87 (0.45-1.30)
China	Cropland	0.52 (0.44-0.61)	0.64 (0.55-0.74)	0.88 (0.78-0.98)
	Natural vegetation	0.06 (0.03-0.09)	0.09 (0.04-0.15)	0.16 (0.04-0.28)

	Total	0.58 (0.46-0.70)	0.74 (0.59-0.89)	1.04 (0.82-1.26)
East China	Cropland	0.44 (0.37-0.51)	0.54 (0.46-0.63)	0.75 (0.66-0.83)
	Natural vegetation	0.04 (0.02-0.07)	0.07 (0.02-0.11)	0.11 (0.03-0.20)
	Total	0.49 (0.39-0.58)	0.61 (0.49-0.73)	0.86 (0.68-1.03)

303   [a]Values are averages with their ranges.
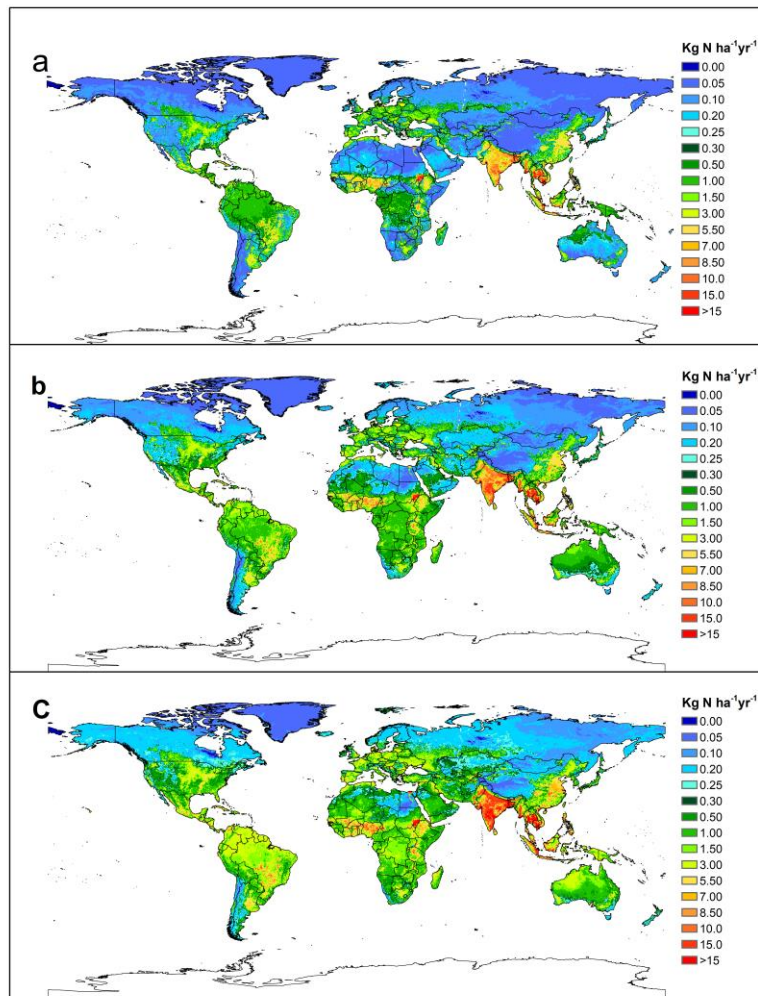
304

305   **Figure 1**. Global spatial distribution of soil emissions of reactive nitrogen gases (HONO, NO,
306   and NO_x) above canopy. a, HONO. b, NO. c, NO_x. The emissions induced by precipitation and
307   fertilization were estimated by an empirical "wetting-drying" method. The figure was created by
308   Kriging interpolation.

309

310   Previous estimations based on the bottom-up ("wetting-drying") approach used in this
311   study showed global emissions of HONO and NO from biological soil crusts of 0.6 and 1.1 Tg N
312   yr^{-1} (Weber et al., 2015), which was consistent with the estimations by a process-based model
313   (0.69 and 1.04 Tg N yr^{-1}) (Porada et al., 2019). We also compared our data with the reported

314   values in previous studies. In general, the estimated soil HONO flux was in the range of reported
315   surface flux measured either in field or laboratory, and also might explain the unknown daytime
316   HONO source (Table S7). Rasool et al. (2019) showed that soil NO+HONO emissions from the
317   eastern United States were in the range of 0–30 ng N m^{-2} s^{-1}, while our calculation was 0–53 ng
318   N m^{-2} s^{-1} (Figure 1). Ren et al. (2011) reported an average HONO flux of -0.056 ± 3.36 ng N m^{-2}
319   s^{-1} above forest canopy by using the relaxed eddy accumulation method, while our calculation
320   was 0.095 ng N m^{-2} s^{-1}. Laufs et al. (2017) reported that daytime HONO flux above an
321   agricultural crop field was in the range of 0.1 to 2.3 ng N m^{-2} s^{-1}, while our estimated soil HONO
322   flux was approximately 2.63 ng N m^{-2} s^{-1} in the same location. Ramsay et al. (2018) reported the
323   HONO flux above an agricultural grassland was in the range of -2.46 to 4.92 ng N m^{-2} s^{-1}, with
324   the maximum achieved after fertilization, while our estimation was 0.92 ng N m^{-2} s^{-1}. The
325   maximum soil HONO flux can even be more than 1000 ng N m^{-2} s^{-1} after fertilization in
326   agricultural field (Tang et al., 2019; Xue et al., 2019). The average agricultural soil HONO flux
327   was in the range of -0.86 to 20.25 ng N m^{-2} s^{-1} measured by field dynamic chambers (Tang et al.,
328   2019), while our estimated value was approximately 8.53 ng N m^{-2} yr^{-1} in the same location. We
329   also compared the soil emissions of NO and NO$_x$ with the reported values, and the results
330   showed good agreement (see more details in Supplementary Text S4).

331

332   3.2 Global soil emissions of HONO using a statistical model related to edaphic factors

333   Soil HONO emissions are controlled by (de)nitrification and other nitrogen cycling
334   processes and are thus affected by soil edaphic factors (Donaldson et al., 2014; Kim & Or, 2019;
335   Maljanen et al., 2013; Oswald et al., 2013; Scharko et al., 2015; Su et al., 2011; Wu et al., 2019).
336   Here, we found that the maximum soil HONO flux ($F_{HONO,max}$) during a wetting-drying cycle
337   was significantly correlated with soil pH, the ratio of total carbon (TC) to total nitrogen (TN), the
338   ratio of nitrite nitrogen (NO$_2^-$-N) to ammonium nitrogen (NH$_4^+$-N), NO$_2^-$-N, sand, and silt
339   content at a global scale (Tables S1 and S8). For HONO emissions from local (Shanghai) soils
340   measured in this study, the controlling factors were more related to soil nitrate nitrogen (NO$_3^-$-
341   N), NO$_2^-$-N, the ratio of total organic carbon (TOC) to NO$_3^-$-N, and NO$_3^-$-N/NH$_4^+$-N (Tables S1
342   and S8). Although Homyak et al. (2015) found unbuffered KCl extractions underestimated NO$_2^-$-
343   N concentration in acidic soil, most of the soil samples in our measurements were alkaline or
344   neutral, and thus it should not affect our results. Furthermore, soil NO$_3^-$-N rather than NO$_2^-$-N
345   content was used in the statistical model, indicating that our conclusions would not be affected.

346   Thus, we established a statistical model to simulate soil HONO emissions ($F_{HONO,model}$)
347   using the above soil edaphic factors and water content (SWC), expressed as equations 11 and 12
348   (see more details in Supplementary Text S5 and Figure S6). This model could accurately predict
349   soil HONO emissions with changes in SWC (Figure S7) and might potentially be applied in the
350   prediction of global seasonal changes in soil HONO emissions. The estimated global soil HONO
351   emissions based on this statistical model were 13.37 (9.29-17.12) Tg N yr^{-1}, with 5.79 (3.84-
352   7.74) Tg N yr^{-1} from cropland (Table 2). This method had much higher emissions from bare land
353   5.23 (4.17-5.98) Tg N yr^{-1} than did the "wetting-drying" model 0.26 (0.17-0.35) Tg N yr^{-1}. The
354   reason could be due to higher HONO emissions at lower soil moisture for bare land (global
355   average approximately 15% WHC) than other land cover soils (global average approximately 30-
356   50% WHC) (Figures S6 and S7). The statistical method also had higher emissions from
357   grassland and wetland than did the "wetting-drying" model, while it had lower emissions from
358   cropland and forest. Nevertheless, the estimated global soil HONO emissions were close to each

359   other, 8.14 and 9.41 Tg N yr^{-1} for the statistical and "wetting-drying" method, respectively, if
360   bare land was not included.

$$F_{HONO,model} = (0.02 + 0.77 * 0.99^{(f(SWC)-f(swc,max))^2}) * F_{LC,HONO,max} \quad (11)$$

$$f(SWC,max) = -5.97 * x_1 + 2.99 * x_2 - 0.02 * x_3 + 53.76 \quad (12)$$

363   where f(SWC) (%) represents the SWC corresponding to the normalized soil HONO flux
364   (the ratio of soil HONO flux to $F_{HONO,max}$); f(SWC,max) (%) represents the simulated SWC
365   corresponding to $F_{HONO,max}$; $F_{LC,HONO,max}$ (ng N m^{-2} s^{-1}) represents the average $F_{HONO,max}$ from
366   different land cover types; and x_1, x_2, and x_3 represent soil pH, TOC (%), and NO$_3^-$-N (mg kg^{-1})
367   content, respectively.

368   **Table 2.** Comparisons of global soil HONO emissions above canopy from cropland, forest,
369   grassland, shrubland, wetland, and bare land calculated by the empirical "wetting-drying"
370   method and statistical model.

371

Land cover	HONO (Tg N yr^{-1})	
	Empirical "wetting-drying" method	Statistical model
Bare land	0.26 (0.17-0.35)[a]	5.23 (4.17-5.98)
Cropland	7.65 (6.30-9.01)	5.79 (3.84-7.74)
Forest	1.12 (0.48-1.76)	0.76 (0.43-1.08)
Grassland	0.60 (0.39-0.81)	1.29 (0.70-1.87)
Shrubland	0.01 [b]	0.11[b]
Wetland	0.02 (0.01-0.04)	0.20 (0.05-0.34)
Total	9.67 (7.36-11.99)	13.37 (9.29-17.12)

372   [a]Values are averages with their ranges.

373   [b]Due to lacking data, the ranges are not available in here.

374

375   3.3 Soil HONO emissions enhanced atmospheric oxidation capacity

376   Based on the WRF-Chem simulations, soil HONO emissions played a more important
377   role in daytime atmospheric HONO concentrations in rural (~20–50%) than urban areas (< 10%,
378   Figure 2). The reasons could be attributed to the larger soil HONO emission rates and smaller
379   contributions from other potential HONO sources in rural areas, where traffic emissions and NO$_2$
380   heterogeneous reactions were both weaker with lower NO$_x$ concentrations (Finlayson-Pitts et al.,
381   2003). Soil HONO emissions mainly enhanced atmospheric HONO and OH concentrations near
382   the ground, while the enhancements were limited above 500 m (Figure 3). For those four soil
383   categories in the study region including cropland, forest, grassland and urban green land, the
384   enhanced daytime HONO concentrations were 0.07 ± 0.02, 0.10 ± 0.06, 0.05 ± 0.03, and 0.03 ±
385   0.01 ppb near the ground, respectively, while the corresponding OH concentrations were
386   enhanced by 0.61 ± 0.18 × 10^6, 0.66 ± 0.44 × 10^6, 0.54 ± 0.32 × 10^6, and 0.15 ± 0.05 × 10^6
387   molecules cm^{-3} near the ground, respectively. Due to the weaker termination by NO$_2$ (NO$_2$ + OH
388   → HNO$_3$) with lower NO$_2$ concentrations, the enhanced OH concentrations by soil HONO
389   emissions (cropland, grassland, and forest) were much larger in rural (30–60%) than those in
390   urban areas (10–20%) (Figures 2 and 3). Detailed information of the impact of soil HONO

391 emissions on OH sources and sinks could be found in Figures 3 and S11. The daily maximum 8-
392 h (DMA8) O_3 enhancements were generally larger in rural (approximately 1.0 ppb) than those in
393 urban areas (approximately 0.5 ppb), while the largest hourly O_3 enhancements reached 1.0–3.0
394 ppb in most part of the region (Figures 2 and 3). Zhang et al. (2016) reported a daily average
395 HONO enhancement of > 1.5 ppb and an O_3 enhancement of 2.4–3.6 ppb after coupling cropland
396 soil HONO emissions (over 100 ng N m^{-2} s^{-1}) into the regional chemical transport model in
397 eastern China. Recently, Wang et al. (2021) reported an O_3 enhancements of 5–6 ppb around
398 noontime with implementing approximately 80 ng N m^{-2} s^{-1} of fertilized soil HONO flux into the
399 CMAQ model. These enhancements were comparable with this study if adopting a smaller soil
400 HONO flux.

401 We also conducted sensitivity simulations by reducing 50% of anthropogenic NO_x
402 emissions, the lower NO_2 concentrations caused less HONO formation via NO_2 heterogeneous
403 reactions and thus increased the contribution of soil HONO emissions to surface HONO
404 concentrations (Figure 2). The spatial patterns of OH enhancements were similar with or without
405 cutting off anthropogenic NO_x emissions, while the DMA8 O_3 enhancements (1.0–1.5 ppb) and
406 the largest hourly O_3 enhancements (2.0–4.0 ppb) were both larger after reducing 50% of
407 anthropogenic NO_x emissions (Figures 2 and 3). Considering the on-going NO_x emission
408 reduction strategy (Zheng et al., 2018) and the concurrent rising O_3 concentrations in China (Li
409 et al., 2019), soil HONO emissions would further increase atmospheric oxidation capacity and
410 O_3 concentrations and play a noticeable role in air quality degradation in the future.
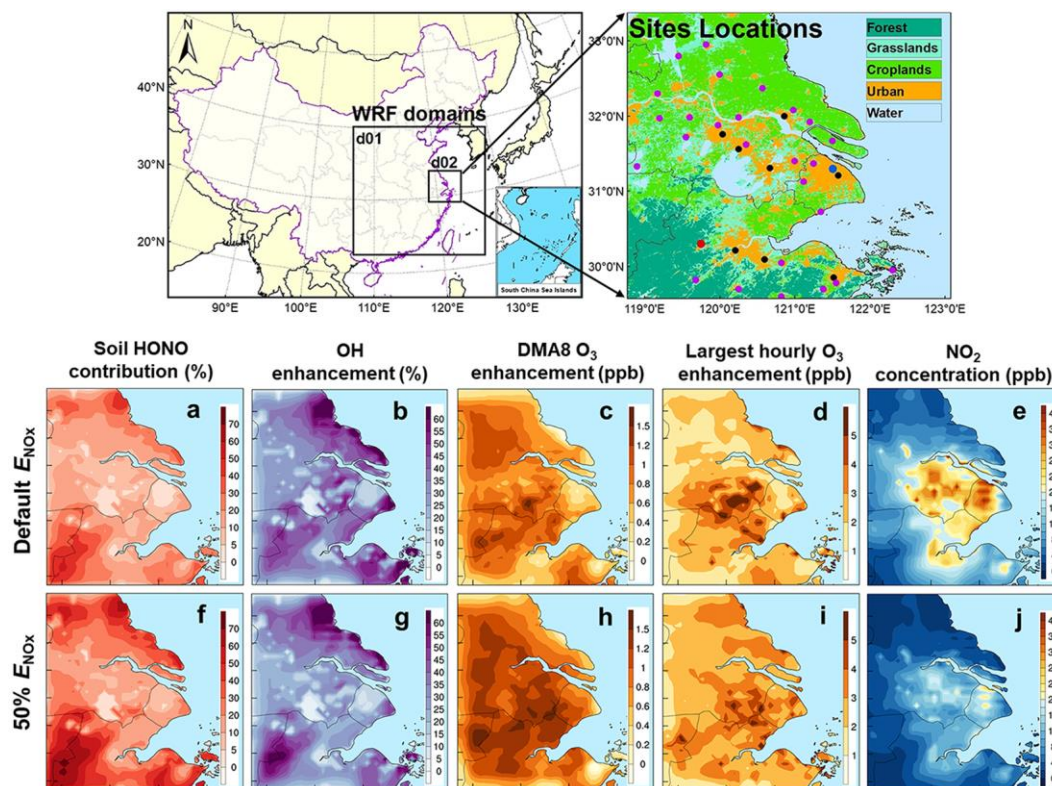

412 **Figure 2**. WRF-Chem domains used in this study and the impact of soil HONO emissions on air
413 quality. The used observational sites (blue dot: HONO; black dots: urban NO_2/O_3; red dot: rural
414 NO_2/O_3 at Lin'an; purple dots: meteorology) are shown in the upper panel. The lower panel
415 shows daytime averaged relative contribution of soil HONO emissions to the five potential

416   HONO sources (a and f), the OH (b and g), the daily maximum 8-h (DMA8) O_3 (c and h) and the
417   largest hourly O_3 (d and i) enhancements compared with the base case, and NO_2 concentrations
418   (e and j) under 100% and 50% NO_x emissions (shown as default and 50% E_{NOx}, respectively) for
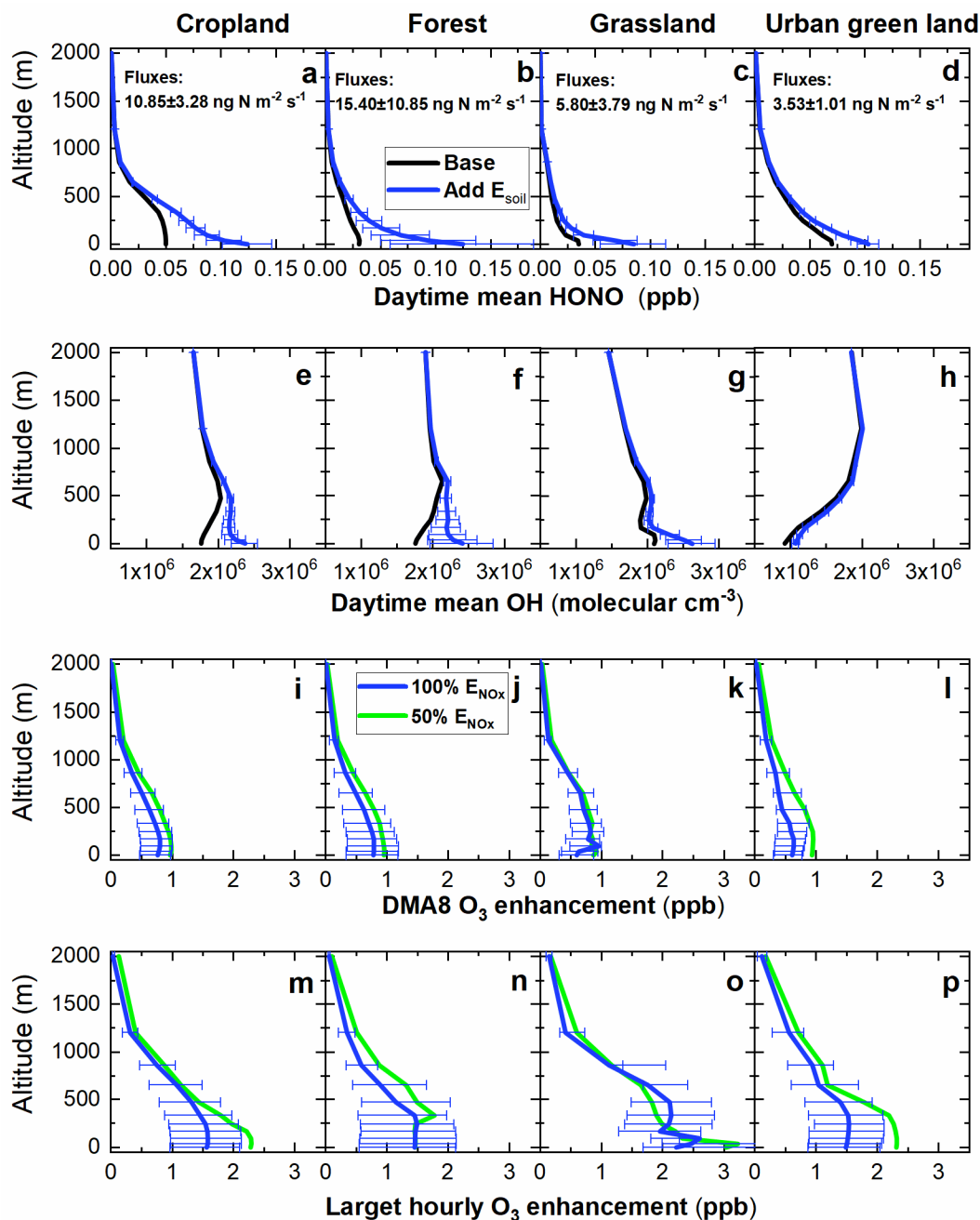419   five typical wetting-drying days in March of 2016.

420

421

422   **Figure 3**. Vertical profiles of simulated HONO and OH concentrations with (cases soil-A, soil-B
423   and soil-C) or without (case base) adding soil HONO emissions (a-f), and the vertical profiles of
424   daily maximum 8-h (DMA8) O_3 enhancement and largest hourly O_3 enhancement induced by

425   soil HONO emissions (i-p). The blue solid line corresponding to the mean soil HONO emissions,
426   the error bar denotes the impacts of the minimum and maximum soil HONO emissions.

427

428   **4 Conclusions**

429   We report global soil HONO emissions estimated by two bottom-up methods, an
430   empirical "wetting-drying" model and a statistical model. Both results were constrained by the
431   limited and inconsistent observed data of soil HONO emissions. More field data on soil HONO
432   emissions from different land cover types, especially from bare land and cropland, could
433   improve the accuracy of the model. For the empirical "wetting-drying" method, global
434   precipitation data were derived from multi-satellite rather than ground-observed data, and the
435   fertilization rates of cropland in each country or province were set to the same value according to
436   the FAO (2017), both of these databases had discrepancies with realistic values and could
437   increase uncertainties. Fertilizer-induced soil HONO emissions from global cropland could
438   increase by 1.75 and 0.1 Tg N yr^{-1}, respectively, when applying gridded fertilizer data from
439   Wang et al. (2019) (including synthetic N fertilizer, livestock manure and crop residues applied
440   to cropland) and Lu & Tian (2017) (including synthetic N fertilizer). For the statistical model,
441   global soil HONO emissions were strongly affected by the resolution and accuracy of soil
442   moisture and physicochemical property (pH, TOC, and NO_3^--N) data. If the maximum soil
443   HONO flux corresponding to soil moisture were well constrained, the results of statistical model
444   should be greatly improved.

445   Soil HONO emissions are controlled by biogeochemical nitrogen cycling, which is
446   affected by nitrogen deposition, temperature, land-use change, and atmospheric carbon dioxide
447   (CO_2) concentrations (Gruber & Galloway, 2008). With climate change and increasing human
448   activities, the land-atmosphere interactions and surface exchange of N_r gases will play more
449   important roles in atmospheric composition and air quality in the future. Based on our
450   simulations, soil HONO emissions accelerated regional HO_x (OH + HO_2) cycling and increased
451   daytime OH concentrations by approximately10–60% and O_3 concentrations by approximately
452   0.5–1.0 ppb. Considering the stronger soil HONO emissions after fertilization processes (Xue et
453   al., 2021), the impact of soil HONO emissions would be even larger during fertilization periods
454   (Wang et al., 2021). By providing global and regional soil emissions of HONO and the impacts
455   on atmospheric chemistry, our work could potentially help biogeochemical and atmospheric
456   chemistry models constrain global soil N_r emissions and the contribution of soil HONO
457   emissions to atmospheric oxidation capacity.

458

465   **Data availability Statement**

466   Global fertilizer data for different countries were obtained from FAOSTAT 2019:
467 Fertilizers by Nutrient domain at http://www.fao.org/faostat/en/#data/RFN. Global daily gridded
468 soil moisture and temperature data in 2018 ($0.25° \times 0.25°$, v201706) were downloaded from the
469 Copernicus Climate Change Service (C3S) Climate Data Store (CDS) at
470 https://cds.climate.copernicus.eu/cdsapp#!/dataset/satellite-soil-moisture?tab=overview. Global
471 monthly gridded soil surface (0-7 cm) temperature data in 2018 ($0.1° \times 0.1°$) were downloaded
472 from the Copernicus Climate Change Service (C3S) Climate Data Store (CDS) at
473 https://cds.climate.copernicus.eu/cdsapp#!/search?text=temperature&keywords=((%20%22Varia
474 ble%20domain:%20Land%20(biosphere)%22%20)%20AND%20(%20%22Spatial%20coverage:
475 %20Global%22%20)). Other data that support the findings of this study are available upon
476 reasonable request from the authors.
477

478 **References**

479 Bernard F., Cazaunau M., Grosselin B., Zhou B., Zheng J., Liang P., Zhang Y., Ye X., Daële V., Mu Y., Zhang R.,
480   Chen J., & Mellouki A. (2016). Measurements of nitrous acid (HONO) in urban area of Shanghai, China.
481   *Environmental Science and Pollution Research*, *23*, 5818-5829. https://doi.org/10.1007/s11356-015-5797-4
482 Bertram T. H., Heckel A., Richter A., Burrows J. P., & Cohen R. C. (2005). Satellite measurements of daily
483   variations in soil NO_x emissions. *Geophysical Research Letters*, *32*, L24812.
484   https://doi.org/10.1029/2005GL024640
485 Ciais P., Sabine C., Bala G., Bopp L., Brovkin V., Canadell J., Chhabra A., DeFries R., Galloway J., Heimann M.,
486   Jones C., Le Quéré C., Myneni R. B., Piao S., & Thornton P. (2013). Carbon and other biogeochemical cycles.
487   In: Stocker T. F., Qin D., Plattner G.-K., Tignor M., Allen S. K., Boschung J., Nauels A., Xia Y., Bex V., &
488   Midgley P. M., editors. Climate change 2013: the physical science basis. Contribution of Working Group I to
489   the Fifth Assessment Report of the Intergovernmental Panel on Climate Change. Cambridge University Press,
490   Cambridge, United Kingdom and New York, NY, USA, pp. 465-570.
491 Crutzen P. J. (1970). The influence of nitrogen oxides on the atmospheric ozone content. *Quarterly Journal of the*
492   *Royal Meteorological Society*, *96*, 320-325. https://doi.org/10.1002/qj.49709640815
493 Donaldson M. A., Bish D. L., & Raff J. D. (2014). Soil surface acidity plays a determining role in the atmospheric-
494   terrestrial exchange of nitrous acid. *Proceedings of the National Academy of Sciences*, *111*, 18472-18477.
495   http://dx.doi.org/10.1073/pnas.1418545112
496 Elshorbany Y. F., Steil B., Brühl C., & Lelieveld J. (2012). Impact of HONO on global atmospheric chemistry
497   calculated with an empirical parameterization in the EMAC model. *Atmospheric Chemistry and Physics*, *12*,
498   9977-10000. https://doi.org/10.5194/acp-12-9977-2012
499 Finlayson-Pitts B. J., Wingen L. M., Sumner A. L., Syomin D., & Ramazan K. A. (2003). The heterogeneous
500   hydrolysis of NO_2 in laboratory systems and in outdoor and indoor atmospheres: An integrated mechanism.
501   *Physical Chemistry Chemical Physics*, *5*, 223-242. https://doi.org/10.1039/B208564J
502 Ganzeveld L. N., Lelieveld J., Dentener F. J., Krol M. C., Bouwman A. J., & Roelofs G.-J. (2002). Global soil-
503   biogenic NO_x emissions and the role of canopy processes. *Journal of Geophysical Research: Atmospheres*, *107*,
504   ACH 9-1-ACH 9-17. https://doi.org/10.1029/2001JD001289
505 Gong P., Liu H., Zhang M., Li C., Wang J., Huang H., Clinton N., Ji L., Li W., Bai Y., Chen B., Xu B., Zhu Z.,
506   Yuan C., Ping Suen H., Guo J., Xu N., Li W., Zhao Y., Yang J., Yu C., Wang X., Fu H., Yu L., Dronova I.,
507   Hui F., Cheng X., Shi X., Xiao F., Liu Q., & Song L. (2019). Stable classification with limited sample:
508   transferring a 30-m resolution sample set collected in 2015 to mapping 10-m resolution global land cover in
509   2017. *Science Bulletin*, *64*, 370-373. https://doi.org/10.1016/j.scib.2019.03.002
510 Gruber N., & Galloway J. N. (2008). An Earth-system perspective of the global nitrogen cycle. *Nature*, *451*, 293-
511   296. https://doi.org/10.1038/nature06592
512 Homyak P. M., Vasquez K. T., Sickman J. O., Parker D. R., & Schimel J. P. (2015). Improving nitrite analysis in
513   soils: drawbacks of the conventional 2 M KCl extraction. *Soil Science Society of America Journal*, *79*, 1237-
514   1242. https://doi.org/10.2136/sssaj2015.02.0061n

515 Huang G., Zhou X., Deng G., Qiao H., & Civerolo K. (2002). Measurements of atmospheric nitrous acid and nitric
516   acid. *Atmospheric Environment*, *36*, 2225-2235. https://doi.org/10.1016/S1352-2310(02)00170-X
517 Hudman R. C., Moore N. E., Mebust A. K., Martin R. V., Russell A. R., Valin L. C., & Cohen R. C. (2012). Steps
518   towards a mechanistic model of global soil nitric oxide emissions: implementation and space based-constraints.
519   *Atmospheric Chemistry and Physics*, *12*, 7779-7795. https://doi.org/10.5194/acp-12-7779-2012
520 Huffman G. J., Stocker E. F., Bolvin D. T., Nelkin E. J., & Tan J. (2019). GPM IMERG Late Precipitation L3 1 day
521   0.1 degree x 0.1 degree V06. In: Savtchenko A., & Greenbelt M., editors. Goddard Earth Sciences Data and
522   Information Services Center (GES DISC), pp. 10.5067/GPM/IMERGDL/DAY/06.
523 Kim M., & Or D. (2019). Microscale pH variations during drying of soils and desert biocrusts affect HONO and
524   NH_3 emissions. *Nature Communications*, *10*, 3944. https://doi.org/10.1038/s41467-019-11956-6
525 Laufs S., Cazaunau M., Stella P., Kurtenbach R., Cellier P., Mellouki A., Loubet B., & Kleffmann J. (2017). Diurnal
526   fluxes of HONO above a crop rotation. *Atmospheric Chemistry and Physics*, *17*, 6907-6923.
527   https://doi.org/10.5194/acp-17-6907-2017
528 Li G., Lei W., Zavala M., Volkamer R., Dusanter S., Stevens P., & Molina L. T. (2010). Impacts of HONO sources
529   on the photochemistry in Mexico City during the MCMA-2006/MILAGO Campaign. *Atmospheric Chemistry
530   and Physics*, *10*, 6551-6567. https://doi.org/10.5194/acp-10-6551-2010
531 Li K., Jacob D. J., Liao H., Shen L., Zhang Q., & Bates K. H. (2019). Anthropogenic drivers of 2013–2017 trends in
532   summer surface ozone in China. *Proceedings of the National Academy of Sciences*, *116*, 422-427.
533   https://doi.org/10.1073/pnas.1812168116
534 Li M., Zhang Q., Kurokawa J. I., Woo J. H., He K., Lu Z., Ohara T., Song Y., Streets D. G., Carmichael G. R.,
535   Cheng Y., Hong C., Huo H., Jiang X., Kang S., Liu F., Su H., & Zheng B. (2017). MIX: a mosaic Asian
536   anthropogenic emission inventory under the international collaboration framework of the MICS-Asia and
537   HTAP. *Atmospheric Chemistry and Physics*, *17*, 935-963. https://doi.org/10.5194/acp-17-935-2017
538 Liang J., Horowitz L. W., Jacob D. J., Wang Y., Fiore A. M., Logan J. A., Gardner G. M., & Munger J. W. (1998).
539   Seasonal budgets of reactive nitrogen species and ozone over the United States, and export fluxes to the global
540   atmosphere. *Journal of Geophysical Research: Atmospheres*, *103*, 13435-13450.
541   https://doi.org/10.1029/97JD03126
542 Lu C., & Tian H. (2017). Global nitrogen and phosphorus fertilizer use for agriculture production in the past half
543   century: shifted hot spots and nutrient imbalance. *Earth Syst. Sci. Data*, *9*, 181-192.
544   https://doi.org/10.5194/essd-9-181-2017
545 Maljanen M., Yli-Pirilä P., Hytönen J., Joutsensaari J., & Martikainen P. J. (2013). Acidic northern soils as sources
546   of atmospheric nitrous acid (HONO). *Soil Biology and Biochemistry*, *67*, 94-97.
547   http://dx.doi.org/10.1016/j.soilbio.2013.08.013
548 Meusel H., Tamm A., Kuhn U., Wu D., Leifke A. L., Fiedler S., Ruckteschler N., Yordanova P., Lang-Yona N.,
549   Pöhlker M., Lelieveld J., Hoffmann T., Pöschl U., Su H., Weber B., & Cheng Y. (2018). Emission of nitrous
550   acid from soil and biological soil crusts represents an important source of HONO in the remote atmosphere in
551   Cyprus. *Atmospheric Chemistry and Physics*, *18*, 799-813. https://doi.org/10.5194/acp-18-799-2018
552 Miyazaki K., Eskes H., Sudo K., Boersma K. F., Bowman K., & Kanaya Y. (2017). Decadal changes in global
553   surface NO_x emissions from multi-constituent satellite data assimilation. *Atmospheric Chemistry and Physics*,
554   *17*, 807-837. https://doi.org/10.5194/acp-17-807-2017
555 Muñoz Sabater J. (2019). ERA5-Land monthly averaged data from 1981 to present. Copernicus Climate Change
556   Service (C3S) Climate Data Store (CDS), Accessed on <15-07-2021>. https://doi.org/10.24381/cds.68d2bb3
557 Oswald R., Behrendt T., Ermel M., Wu D., Su H., Cheng Y., Breuninger C., Moravek A., Mougin E., Delon C.,
558   Loubet B., Pommerening-Röser A., Sörgel M., Pöschl U., Hoffmann T., Andreae M. O., Meixner F. X., &
559   Trebs I. (2013). HONO emissions from soil bacteria as a major source of atmospheric reactive nitrogen.
560   *Science*, *341*, 1233-1235. https://doi.org/10.1126/science.1242266
561 Pinder R. W., Davidson E. A., Goodale C. L., Greaver T. L., Herrick J. D., & Liu L. (2012). Climate change impacts
562   of US reactive nitrogen. *Proceedings of the National Academy of Sciences*, *109*, 7671-5.
563   https://doi.org/10.1073/pnas.1114243109
564 Plake D., Stella P., Moravek A., Mayer J. C., Ammann C., Held A., & Trebs I. (2015). Comparison of ozone
565   deposition measured with the dynamic chamber and the eddy covariance method. *Agricultural and Forest
566   Meteorology*, *206*, 97-112. https://doi.org/10.1016/j.agrformet.2015.02.014
567 Porada P., Tamm A., Raggio J., Cheng Y., Kleidon A., Pöschl U., & Weber B. (2019). Global NO and HONO
568   emissions of biological soil crusts estimated by a process-based non-vascular vegetation model.
569   *Biogeosciences*, *16*, 2003-2031. https://doi.org/10.1016/10.5194/bg-16-2003-2019

Ramsay R., Di Marco C. F., Heal M. R., Twigg M. M., Cowan N., Jones M. R., Leeson S. R., Bloss W. J., Kramer L. J., Crilley L., Sörgel M., Andreae M., & Nemitz E. (2018). Surface–atmosphere exchange of inorganic water-soluble gases and associated ions in bulk aerosol above agricultural grassland pre- and postfertilisation. *Atmospheric Chemistry and Physics*, *18*, 16953-16978. https://doi.org/10.5194/acp-18-16953-2018

Rasool Q. Z., Bash J. O., & Cohan D. S. (2019). Mechanistic representation of soil nitrogen emissions in the Community Multiscale Air Quality (CMAQ) model v 5.1. *Geosci. Model Dev.*, *12*, 849-878. https://doi.org/10.5194/gmd-12-849-2019

Ren X., Sanders J. E., Rajendran A., Weber R. J., Goldstein A. H., Pusede S. E., Browne E. C., Min K. E., & Cohen R. C. (2011). A relaxed eddy accumulation system for measuring vertical fluxes of nitrous acid. *Atmospheric Measurement Techniques*, *4*, 2093-2103. https://doi.org/10.5194/amt-4-2093-2011

Rummel, U., Ammann, C., Gut, A., Meixner, F. X., & Andreae M. O. (2002). Eddy covariance measurements of nitric oxide flux within an Amazonian rain forest. *Journal of Geophysical Research: Atmospheres*, *107*, LBA 17-1-LBA 17-9. https://doi.org/10.1029/2001JD000520

Scharko N. K., Schütte U. M. E., Berke A. E., Banina L., Peel H. R., Donaldson M. A., Hemmerich C., White J. R., & Raff J. D. (2015). Combined flux chamber and genomics approach links nitrous acid emissions to ammonia oxidizing bacteria and archaea in urban and agricultural soil. *Environmental Science & Technology*, *49*, 13825-13834. https://doi.org/10.1021/acs.est.5b00838

Shangguan W., Dai Y., Duan Q., Liu B., & Yuan H. (2014). A global soil data set for earth system modeling. *Journal of Advances in Modeling Earth Systems*, *6*, 249-263. https://doi.org/10.1002/2013MS000293

Sörgel M., Trebs I., Wu D., & Held A. (2015). A comparison of measured HONO uptake and release with calculated source strengths in a heterogeneous forest environment. *Atmospheric Chemistry and Physics*, *15*, 9237-9251. https://doi.org/10.5194/acp-15-9237-2015

Steinkamp J., & Lawrence M. G. (2011). Improvement and evaluation of simulated global biogenic soil NO emissions in an AC-GCM. *Atmospheric Chemistry and Physics*, *11*, 6063-6082. https://doi.org/10.5194/acp-11-6063-2011

Su H., Cheng Y., Oswald R., Behrendt T., Trebs I., Meixner F. X., Andreae M. O., Cheng P., Zhang Y., & Pöschl U. (2011). Soil nitrite as a source of atmospheric HONO and OH radicals. *Science*, *333*, 1616-1618. https://doi.org/10.1126/science.1207687

Tang K., Qin M., Duan J., Fang W., Meng F., Liang S., Xie P., Liu J., Liu W., Xue C., & Mu Y. (2019). A dual dynamic chamber system based on IBBCEAS for measuring fluxes of nitrous acid in agricultural fields in the North China Plain. *Atmospheric Environment*, *196*, 10-19. https://doi.org/10.1016/j.atmosenv.2018.09.059

Tang K., Qin M., Fang W., Duan J., Meng F., Ye K., Zhang H., Xie P., He Y., Xu W., Liu J., & Liu W. (2020). Simultaneous detection of atmospheric HONO and NO_2 utilising an IBBCEAS system based on an iterative algorithm. *Atmos. Meas. Tech.*, *13*, 6487-6499. https://doi.org/10.5194/amt-13-6487-2020

van Dijk S. M., Gut A., Kirkman G. A., Meixner F. X., Andreae M. O., & Gomes B. M. (2002). Biogenic NO emissions from forest and pasture soils: Relating laboratory studies to field measurements. *Journal of Geophysical Research*, *107*. https://doi.org/10.1029/2001jd000358

VandenBoer T. C., Young C. J., Talukdar R. K., Markovic M. Z., Brown S. S., Roberts J. M., & Murphy J. G. (2015). Nocturnal loss and daytime source of nitrous acid through reactive uptake and displacement. *Nature Geoscience*, *8*, 55-60. https://doi.org/10.1038/ngeo2298

Vinken G. C. M., Boersma K. F., Maasakkers J. D., Adon M., & Martin R. V. (2014). Worldwide biogenic soil NO_x emissions inferred from OMI NO_2 observations. *Atmospheric Chemistry and Physics*, *14*, 10363-10381. https://doi.org/10.5194/acp-14-10363-2014

Wang Q., Zhou F., Shang Z., Ciais P., Winiwarter W., Jackson R. B., Tubiello F. N., Janssens-Maenhout G., Tian H., Cui X., Canadell J. G., Piao S., & Tao S. (2019). Data-driven estimates of global nitrous oxide emissions from croplands. *National Science Review*, *7*, 441-452. https://doi.org/10.1093/nsr/nwz087

Wang Y., Fu X., Wu D., Wang M., Lu K., Mu Y., Liu Z., Zhang Y., & Wang T. (2021). Agricultural fertilization aggravates air pollution by stimulating soil nitrous acid emissions at high soil moisture. *Environmental Science & Technology*, *55*, 14556-14566. https://doi.org/10.1021/acs.est.1c04134

Weber B., Wu D., Tamm A., Ruckteschler N., Rodríguez-Caballero E., Steinkamp J., Meusel H., Elbert W., Behrendt T., Sörgel M., Cheng Y., Crutzen P. J., Su H., & Pöschl U. (2015). Biological soil crusts accelerate the nitrogen cycle through large NO and HONO emissions in drylands. *Proceedings of the National Academy of Sciences*, *112*, 15384-15389. https://doi.org/10.1073/pnas.1515818112

Winkler J. P., Cherry R. S., & Schlesinger W. H. (1996). The Q_{10} relationship of microbial respiration in a temperate forest soil. *Soil Biology and Biochemistry*, *28*, 1067-1072. https://doi.org/10.1016/0038-0717(96)00076-4

625　Wu D., Deng L., Liu Y., Xi D., Zou H., Wang R., Sha Z., Pan Y., Hou L., & Liu M. (2020). Comparisons of the
626　　　effects of different drying methods on soil nitrogen fractions: Insights into emissions of reactive nitrogen gases
627　　　(HONO and NO). *Atmospheric and Oceanic Science Letters*, *13*, 224-231.
628　　　https://doi.org/10.1080/16742834.2020.1733388
629　Wu D., Horn M. A., Behrendt T., Müller S., Li J., Cole J. A., Xie B., Ju X., Li G., Ermel M., Oswald R., Fröhlich-
630　　　Nowoisky J., Hoor P., Hu C., Liu M., Andreae M. O., Pöschl U., Cheng Y., Su H., Trebs I., Weber B., &
631　　　Sörgel M. (2019). Soil HONO emissions at high moisture content are driven by microbial nitrate reduction to
632　　　nitrite: tackling the HONO puzzle. *The ISME Journal*, *13*, 1688-1699. https://doi.org/10.1038/s41396-019-
633　　　0379-y
634　Xu-Ri, & Prentice I. C. (2008). Terrestrial nitrogen cycle simulation with a dynamic global vegetation model.
635　　　*Global Change Biology*, *14*, 1745-1764. https://doi.org/10.1111/j.1365-2486.2008.01625.x
636　Xue C., Ye C., Zhang C., Catoire V., Liu P., Gu R., Zhang J., Ma Z., Zhao X., Zhang W., Ren Y., Krysztofiak G.,
637　　　Tong S., Xue L., An J., Ge M., Mellouki A., & Mu Y. (2021). Evidence for strong HONO emission from
638　　　fertilized agricultural fields and its remarkable impact on regional O_3 pollution in the summer North China
639　　　Plain. *ACS Earth and Space Chemistry*, *5*, 340-347. https://doi.org/10.1021/acsearthspacechem.0c00314
640　Xue C., Ye C., Zhang Y., Ma Z., Liu P., Zhang C., Zhao X., Liu J., & Mu Y. (2019). Development and application
641　　　of a twin open-top chambers method to measure soil HONO emission in the North China Plain. *Science of the
642　　　Total Environment*, *659*, 621-631. https://doi.org/10.1016/j.scitotenv.2018.12.245
643　Yan X., Ohara T., & Akimoto H. (2005). Statistical modeling of global soil NO_x emissions. *Global Biogeochemical
644　　　Cycles*, *19*, GB3019. https://doi.org/10.1029/2004GB002276
645　Yienger J. J., & Levy II H. (1995). Empirical model of global soil-biogenic NO_x emissions. *Journal of Geophysical
646　　　Research: Atmospheres*, *100*, 11447-11464. https://doi.org/10.1029/95JD00370
647　Zhang J., An J., Qu Y., Liu X., & Chen Y. (2019). Impacts of potential HONO sources on the concentrations of
648　　　oxidants and secondary organic aerosols in the Beijing-Tianjin-Hebei region of China. *Science of the Total
649　　　Environment*, *647*, 836-852. https://doi.org/10.1016/j.scitotenv.2018.08.030
650　Zhang L., Wang T., Zhang Q., Zheng J., Xu Z., & Lv M. (2016). Potential sources of nitrous acid (HONO) and their
651　　　impacts on ozone: A WRF-Chem study in a polluted subtropical region. *Journal of Geophysical Research:
652　　　Atmospheres*, *121*, 3645-3662. https://doi.org/10.1002/2015JD024468
653　Zheng B., Tong D., Li M., Liu F., Hong C., Geng G., Li H., Li X., Peng L., Qi J., Yan L., Zhang Y., Zhao H., Zheng
654　　　Y., He K., & Zhang Q. (2018). Trends in China's anthropogenic emissions since 2010 as the consequence of
655　　　clean air actions. *Atmospheric Chemistry and Physics*, *18*, 14095-14111. https://doi.org/10.5194/acp-18-14095-
656　　　2018
657　Zhu Z., Bi J., Pan Y., Ganguly S., Anav A., Xu L., Samanta A., Piao S., Nemani R. R., & Myneni R. B. (2013).
658　　　Global data sets of vegetation leaf area index (LAI)3g and fraction of photosynthetically active radiation
659　　　(FPAR)3g derived from Global Inventory Modeling and Mapping Studies (GIMMS) normalized difference
660　　　vegetation index (NDVI3g) for the period 1981 to 2011. *Remote Sensing*, *5*, 927-948.
661　　　https://doi.org/10.3390/rs5020927
662

References from the Supporting Information

664　Bhattarai H. R., Liimatainen M., Nykänen H., Kivimäenpää M., Martikainen P. J., & Maljanen M. (2019).
665　　　Germinating wheat promotes the emission of atmospherically significant nitrous acid (HONO) gas from soils.
666　　　*Soil Biology and Biochemistry*, *136*, 107518. https://doi.org/10.1016/j.soilbio.2019.06.014
667　Crippa M., Guizzardi D., Muntean M., Schaaf E., Dentener F., van Aardenne J. A., Monni S., Doering U., Olivier J.
668　　　G. J., Pagliari V., & Janssens-Maenhout G. (2018). Gridded emissions of air pollutants for the period 1970–
669　　　2012 within EDGAR v4.3.2. *Earth System Science Data*, *10*, 1987-2013. https://doi.org/10.5194/essd-10-1987-
670　　　2018
671　Gu B., Ju X., Chang J., Ge Y., & Vitousek P. M. (2015). Integrated reactive nitrogen budgets and future trends in
672　　　China. *Proceedings of the National Academy of Sciences*, *112*, 8792-8797.
673　　　https://doi.org/10.1073/pnas.1510211112
674　Hickman J. E., Huang Y., Wu S., Diru W., Groffman P. M., Tully K. L., & Palm C. A. (2017). Nonlinear response
675　　　of nitric oxide fluxes to fertilizer inputs and the impacts of agricultural intensification on tropospheric ozone
676　　　pollution in Kenya. *Global Change Biology*, *23*, 3193-3204. https://doi.org/10.1111/gcb.13644

677 Huang Y., & Li D. (2014). Soil nitric oxide emissions from terrestrial ecosystems in China: a synthesis of modeling
678   and measurements. *Scientific Reports*, *4*, 7406. https://doi.org/10.1038/srep07406
679 Li L., Chen C. H., Huang C., Huang H. Y., Zhang G. F., Wang Y. J., Wang H. L., Lou S. R., Qiao L. P., Zhou M.,
680   Chen M. H., Chen Y. R., Streets D. G., Fu J. S., & Jang C. J. (2012). Process analysis of regional ozone
681   formation over the Yangtze River Delta, China using the Community Multi-scale Air Quality modeling system.
682   *Atmospheric Chemistry and Physics*, *12*, 10971-10987. https://doi.org/10.5194/acp-12-10971-2012
683 Lin J. T. (2012). Satellite constraint for emissions of nitrogen oxides from anthropogenic, lightning and soil sources
684   over East China on a high-resolution grid. *Atmospheric Chemistry and Physics*, *12*, 2881-2898.
685   https://doi.org/10.5194/acp-12-2881-2012
686 Lin Y.-L., Farley R. D., & Orville H. D. (1983). Bulk Parameterization of the Snow Field in a Cloud Model. *Journal*
687   *of Applied Meteorology and Climatology*, *22*, 1065-1092. https://doi.org/10.1175/1520-
688   0450(1983)022<1065:Bpotsf>2.0.Co;2
689 Liu S., Lin F., Wu S., Ji C., Sun Y., Jin Y., Li S., Li Z., & Zou J. (2017). A meta-analysis of fertilizer-induced soil
690   NO and combined $NO+N_2O$ emissions. *Global Change Biology*, *23*, 2520-2532.
691   https://doi.org/10.1111/gcb.13485
692 Mei B., Zheng X., Xie B., Dong H., Zhou Z., Wang R., Deng J., Cui F., Tong H., & Zhu J. (2009). Nitric oxide
693   emissions from conventional vegetable fields in southeastern China. *Atmospheric Environment*, *43*, 2762-2769.
694   https://doi.org/10.1016/j.atmosenv.2009.02.040
695 Mushinski R. M., Phillips R. P., Payne Z. C., Abney R. B., Jo I., Fei S., Pusede S. E., White J. R., Rusch D. B., &
696   Raff J. D. (2019). Microbial mechanisms and ecosystem flux estimation for aerobic NO_y emissions from
697   deciduous forest soils. *Proceedings of the National Academy of Sciences*, *116*, 2138-2145.
698   https://doi.org/10.1073/pnas.1814632116
699 Palmer K., Drake H. L., & Horn M. A. (2010). Association of novel and highly diverse acid-tolerant denitrifiers
700   with N_2O fluxes of an acidic fen. *Applied and Environmental Microbiology*, *76*, 1125-1134.
701   https://doi.org/10.1128/AEM.02256-09
702 Pilegaard K. (2013). Processes regulating nitric oxide emissions from soils. *Philosophical Transactions of the Royal*
703   *Society B: Biological Sciences*, *368*, 20130126. https://doi.org/10.1098/rstb.2013.0126
704 Ryan R. G., Rhodes S., Tully M., Wilson S., Jones N., Frieß U., & Schofield R. (2018). Daytime HONO, NO_2 and
705   aerosol distributions from MAX-DOAS observations in Melbourne. *Atmospheric Chemistry and Physics*, *18*,
706   13969-13985. https://doi.org/10.5194/acp-18-13969-2018
707 Stutz J., Alicke B., & Neftel A. (2002). Nitrous acid formation in the urban atmosphere: Gradient measurements of
708   NO_2 and HONO over grass in Milan, Italy. *Journal of Geophysical Research: Atmospheres*, *107*, 8192.
709   https://doi.org/10.1029/2001JD000390
710 Tsai C., Spolaor M., Colosimo S. F., Pikelnaya O., Cheung R., Williams E., Gilman J. B., Lerner B. M., Zamora R.
711   J., Warneke C., Roberts J. M., Ahmadov R., de Gouw J., Bates T., Quinn P. K., & Stutz J. (2018). Nitrous acid
712   formation in a snow-free wintertime polluted rural area. *Atmospheric Chemistry and Physics*, *18*, 1977-1996.
713   https://doi.org/10.5194/acp-18-1977-2018
714 Wang F., An J., Li Y., Tang Y., Lin J., Qu Y., Chen Y., Zhang B., & Zhai J. (2014). Impacts of uncertainty in
715   AVOC emissions on the summer RO_x budget and ozone production rate in the three most rapidly-developing
716   economic growth regions of China. *Advances in Atmospheric Sciences*, *31*, 1331-1342.
717   https://doi.org/10.1007/s00376-014-3251-z
718 Wang Q. g., Han Z., & Higano Y. (2005). An inventory of nitric oxide emissions from soils in China. *Environmental*
719   *Pollution*, *135*, 83-90. https://doi.org/10.1016/j.envpol.2004.10.007
720 Wang X., Zhang Y., Hu Y., Zhou W., Lu K., Zhong L., Zeng L., Shao M., Hu M., & Russell A. G. (2010). Process
721   analysis and sensitivity study of regional ozone formation over the Pearl River Delta, China, during the
722   PRIDE-PRD2004 campaign using the Community Multiscale Air Quality modeling system. *Atmospheric*
723   *Chemistry and Physics*, *10*, 4423-4437. https://doi.org/10.5194/acp-10-4423-2010
724 Wong K. W., Tsai C., Lefer B., Haman C., Grossberg N., Brune W. H., Ren X., Luke W., & Stutz J. (2012).
725   Daytime HONO vertical gradients during SHARP 2009 in Houston, TX. *Atmospheric Chemistry and Physics*,
726   *12*, 635-652. https://doi.org/10.5194/acp-12-635-2012
727 Wu D., Kampf C. J., Pöschl U., Oswald R., Cui J., Ermel M., Hu C., Trebs I., & Sörgel M. (2014). Novel tracer
728   method to measure isotopic labeled gas-phase nitrous acid ($HO^{15}NO$) in biogeochemical studies.
729   *Environmental Science & Technology*, *48*, 8021-8027. https://doi.org/10.1021/es501353x
730 Xu P., Chen A., Houlton B. Z., Zeng Z., Wei S., Zhao C., Lu H., Liao Y., Zheng Z., Luan S., & Zheng Y. (2020).
731   Spatial variation of reactive nitrogen emissions from China's croplands codetermined by regional urbanization

732   and its feedback to global climate change. *Geophysical Research Letters*, *47*, e2019GL086551.
733   https://doi.org/10.1029/2019GL086551
734 Zhang H., Li J., Ying Q., Yu J. Z., Wu D., Cheng Y., He K., & Jiang J. (2012). Source apportionment of PM2.5
735   nitrate and sulfate in China using a source-oriented chemical transport model. *Atmospheric Environment*, *62*,
736   228-242. https://doi.org/10.1016/j.atmosenv.2012.08.014
737 Zhou X., Zhang N., TerAvest M., Tang D., Hou J., Bertman S., Alaghmand M., Shepson P. B., Carroll M. A.,
738   Griffith S., Dusanter S., & Stevens P. S. (2011). Nitric acid photolysis on forest canopy surface as a source for
739   tropospheric nitrous acid. *Nature Geoscience*, *4*, 440-443. https://doi.org/10.1038/ngeo1164

740